Journal of Materials Chemistry A

ROYAL SOCIETY OF CHEMISTRY

PAPER

View Article Online
View Journal | View Issue

Cite this: J. Mater. Chem. A, 2024, 12, 16854

Dy_2NiRuO_6 perovskite with high activity and durability for the oxygen evolution reaction in acidic electrolyte†

Isabel Rodríguez-García, [a] José Luis Gómez de la Fuente,[a] Dmitry Galyamin, [a] Álvaro Tolosana-Moranchel,[a] Paula Kayser, [bc] Mohamed Abdel Salam, [d] José Antonio Alonso, [b] Federico Calle-Vallejo,[ef] Sergio Rojas *[a] and María Retuerto *[a]

Ru mixed oxides may be suitable materials to replace state-of-the-art Ir-based catalysts in the anode of proton exchange membrane electrolyzers. To do this, the activity and especially the durability of Ru for the oxygen evolution reaction (OER) in acidic electrolyte should be improved. This work reports a family of Ru-based perovskites that combines both high activity and durability for the OER in acidic electrolyte. R_2NiRuO_6 double perovskites with R^{3+} = Pr^{3+}, Nd^{3+}, Tb^{3+}, Dy^{3+}, Y^{3+}, Ho^{3+} and Er^{3+}, and with Ni^{2+} and Ru^{4+} occupying B and B′ positions have been synthesized and evaluated for the OER in acidic electrolyte. The OER activities of R_2NiRuO_6 mixed oxides depend on the nature of R^{3+}, with Dy_2NiRuO_6 displaying the highest activity (1.507 V at 10 mA cm^{-2}) and being stable for more than 400 consecutive OER cycles measured at a slow scan rate. Characterization data indicate that the shorter Ru–O bonds in Dy_2NiRuO_6 are beneficial for the OER performance compared to the rest of the series. Computational modelling shows that Ru sites at pristine Dy_2NiRuO_6 are highly active for the OER, and their activity increases slightly upon Dy dissolution and progressively decreases as the local ratio of Ni to Ru is lowered.

Received 6th November 2023
Accepted 26th May 2024

DOI: 10.1039/d3ta06788b

rsc.li/materials-a

Introduction

Green hydrogen produced by the electrolysis of water using renewable energies is expected to assume a leading role in the transition toward a decarbonized society. Among the available electrolysis technologies, polymer electrolyte membrane water electrolysis (PEMWE) presents several benefits, such as its operation at significantly high current densities (>2 A cm^{-2}), thus reducing the operational costs and increasing H_2 production; lower gas crossover rate, yielding nearly pure H_2; and compact design, fast response and smaller carbon footprint.[1]

Water electrolysis is the splitting of H_2O into H_2 and O_2 by applying electricity. In a PEMWE, H_2 is produced at the cathode ($4H^+ + 4e^- \rightarrow 2H_2$, hydrogen evolution, HER), while O_2 is produced at the anode ($2H_2O \rightarrow O_2 + 4H^+ + 4e^-$, oxygen evolution, OER).[2] The latter reaction is the limiting process of water electrolysis, and its efficiency depends strongly on the electrocatalyst. Therefore, the nature of the electrocatalyst should be considered carefully to accelerate the reaction kinetics and reduce the overpotential. The harsh environment of the OER in a PEMWE, characterized by high voltage, low bulk and local pH and high pO_2 ultimately determines the catalysts that can be used.[3] In fact, currently only iridium catalysts are used commercially and relatively large Ir loadings are required to produce fair amounts of hydrogen. Ir is a scarce and expensive element. Consequently, the costs of PEMWEs and the green hydrogen they produce are currently high.[4,5] Recent studies have shown that a significant decrease in Ir content without activity penalties is possible by using Ir mixed oxides.[6,7]

An alternative to Ir is the use of Ru-based anode electrocatalysts. Ru is more affordable, abundant and active than Ir. In fact, lower overpotentials are required to achieve similar current densities when using Ru compared to Ir. However, Ru catalysts have severe stability problems in acidic media because of the

[a]Grupo de Energía y Química Sostenibles, Instituto de Catálisis y Petroleoquímica, CSIC, C/Marie Curie 2, 28049, Madrid, Spain. E-mail: m.retuerto@csic.es
[b]Instituto de Ciencia de Materiales de Madrid, CSIC, C/Sor Juana Inés de la Cruz 3, 28049 Madrid, Spain
[c]Dep. Q. Inorgánica I, Facultad Químicas, Universidad Complutense, Avda. Complutense s/n, 28040-Ciudad Universitaria, Madrid, Spain
[d]Chemistry Department, Faculty of Science, King Abdulaziz University, P. O Box 80200, Jeddah, 21589, Saudi Arabia
[e]Nano-Bio Spectroscopy Group and European Theoretical Spectroscopy Facility (ETSF), Department of Advanced Materials and Polymers: Physics, Chemistry and Technology, University of the Basque Country UPV/EHU, Avenida Tolosa 72, 20018 San Sebastián, Spain
[f]IKERBASQUE, Basque Foundation for Science, Plaza de Euskadi 5, 48009 Bilbao, Spain

† Electronic supplementary information (ESI) available. See DOI: https://doi.org/10.1039/d3ta06788b

dissolution of highly oxidized Ru species, *e.g.* RuO_4, under the harsh conditions of the OER at high voltages (>1.4 V).[8] Therefore, it is imperative to design Ru phases with structures that prevent Ru dissolution during the OER while displaying high activity. Only then can the loading of Ru be substantially reduced on PEMWE anodes.

Several Ru pyrochlores ($R_2Ru_2O_7$) with enhanced OER durability have been reported recently.[9–12] These studies suggest that the environment of Ru cations in the oxide structure plays a determining role in the durability and stability of Ru oxides. Our group recently reported a family of R_2MnRuO_7 pyrochlores, which contains half as much Ru than typical pyrochlores but displays greater OER performance.[13] Interestingly, the Ru environment in such pyrochlores is octahedral, similar to that exhibited in perovskites. However, the Ru perovskites hitherto reported display lower stability than Ru pyrochlores. For instance, $SrRuO_3$ lasts only a few cycles[14] and its doping with alkali elements improved its stability only up to 80 OER cycles and at relatively low potentials.[15,16] Rapid deactivation stems from the dissolution of Sr followed by that of Ru.

In this work, we investigate Ru double perovskites without Sr^{2+} or alkali cations to improve the stability of the catalysts, maintaining Ru^{4+} in an octahedral environment. R_2NiRuO_6 with low Ru content is studied (R = Pr, Nd, Tb, Dy, Y, Ho, and Er). The catalysts are characterized by electrochemical and physicochemical techniques and exhibit salient OER performance, especially Dy_2NiRuO_6. Computational modelling illustrates how Dy and Ni dissolution modulates the OER performance of the latter double perovskite.

Experimental

Synthesis of R_2NiRuO_6

R_2NiRuO_6 oxides were synthesized by wet chemistry. Using the citrate method, highly reactive precursors are obtained, which lowers the final synthesis temperatures. Stoichiometric amounts of Dy_2O_3, Er_2O_3, Ho_2O_3, Nd_2O_3, Pr_6O_{11}, Tb_2O_3, Y_2O_3 and $Ni(NO_3)_2 \cdot 6H_2O$ are dissolved by magnetic stirring in a volume of 250 mL of 10% citric acid aqueous solution to which 5 mL of HNO_3 are added. RuO_2 remained in a suspension without dissolving. The solution is gently stirred and heated at 100 °C for the production of organic resins containing a homogeneous distribution of the cations involved. After evaporation of water, the resins are dried at 140 °C and then heated at 600 °C for 12 h (rate: 2 °C min^{-1}) to decompose organic materials and remove nitrates. This treatment gives rise to highly reactive precursor materials that are finally heated in air at high temperature to obtain the pure phases of each compound. Dy and Tb perovskites are treated at 1100 °C/12 h + 1100 °C/12 h to obtain pure samples; Nd and Pr needed only 1100 °C/12 h, and finally Er, Ho and Y needed 1300 °C/12 h.

Characterization

Phase identification and crystal size are determined by X-ray powder diffraction (XRD) in the Bragg–Brentano reflection geometry with CuKα radiation (λ = 1.5418 Å). The crystal structures are analyzed with the Rietveld method using the Fullprof program.[17,18] In the refinements, a pseudo-Voigt function is used for the shape of the peaks.

TEM images, high-resolution electron microscopy (HRTEM) and X-ray energy dispersive spectra (EDX) are recorded using a JEOL 2100 field emission gun transmission electron microscope operating at 200 kV and equipped with an EDX (X-Max80 by Oxford Instruments). Specimens are prepared by depositing the samples on top of a Cu grid supporting a lacey carbon film.

X-ray photoelectron spectra (XPS) are recorded using a SPECS GmbH with a UHV system (pressure approx. 10–10 mbar), with a PHOIBOS 150 9MCD energy analyzer, monochromatic (with a double Al/Ag anode) and non-monochromatic (with a double Al/Ag anode) X-ray sources, an electron source for charge compensation, a UV photon source, an ion source and a sample pretreatment chamber (HPC). Peak analysis was conducted using the CasaXPS processing software, using a combination of Gaussian and Lorentzian peaks and a Shirley background. Asymmetric peaks were used for the fitting of the Ru 3d peaks. The C 1s peak was set at 284.6 eV and used as the reference.

Electrochemical measurements

An Autolab PGstat 302 N potentiostat/galvanostat is used to perform the electrochemical measurements. A three-compartment glass cell and a rotating disk electrode (RDE) (Pine Research Instruments) are used. A graphite bar is used as the counter electrode and Ag/AgCl 3.5 M is used as the reference electrode. In this manuscript, all potentials are referred to the reversible hydrogen electrode (RHE). The following equation was used to convert the potentials: $E_{RHE} = E\,(Ag/AgCl) + E^0\,(Ag/AgCl) + 0.059\,pH$. The electrochemically active surface area (ECSA) was calculated by measuring the non-faradaic capacitive current associated with the double-layer charging of R_2NiRuO_6 (without active carbon) at different scan rates or by Electrochemical Impedance Spectroscopy (EIS).[19]

The R_2NiRuO_6 catalysts are deposited on the electrode in the form of an ink, which is prepared with 5 mg of the catalyst and 1 mg of Vulcan-XC-72R (carbon black) to improve the electrochemical conductivity. The mixture is dispersed in tetrahydrofuran (THF) and 5% Nafion and sonicated using a UP50H ultrasonic processor (Hielscher). The ink composition is 5 mg_{oxide}, 1 mg_{vulcan}, 0.03 mL_{Nafion}, and 0.97 mL_{THF}. 10 μL of ink are deposited on the electrode with an area of 0.196 cm^2, with a catalyst loading of 0.255 mg_{oxide} cm^{-2}.

The voltammograms for the OER are recorded at 10 mV s^{-1} between 1.1 and 1.7 V. Measurements are performed in an electrolyte of 0.1 M $HClO_4$ saturated with O_2 to ensure O_2/H_2O equilibrium at 1.23 V, at a rotational speed of 1600 rpm. The OER kinetic curves are corrected for capacitance using the average of the anodic and cathodic curves and corrected for *iR* using the formula $E\text{-}iR_{corrected} = E_{applied} - iR$. In this formula, i is the current and R is the ohmic electrolyte resistance ($R \sim 25\ \Omega$), calculated from the intercept of the high frequency region of the EIS spectrum with the x-axis of the Nyquist plot at open voltage. The durability of the catalysts is evaluated by performing 100 OER cycles measured at 10 mV s^{-1} between 1.1 and 1.7 V.

Computational modelling

The DFT calculations were made with VASP,[20] the PBE exchange-correlation functional[21] and the projector augmented-wave (PAW) method.[22] We used Dudarev *et al.*'s GGA + U approach,[23] with $U_{eff} = 6.70$ eV[24] for Ru, and $U_{eff} = 6.01$ eV for Ni.[25] All geometry optimizations were spin unrestricted and used a plane-wave cutoff of 400 eV, and the atoms were relaxed until the residual forces were <0.05 eV Å^{-1}. To simulate Dy and Ni dissolution, we sequentially removed these species from the pristine double perovskite structure, as shown in Section S5.† The converged coordinates of all slabs are given in Section S5 in the ESI.† The OER proceeds as a series of proton-electron transfers transforming water into oxygen as $H_2O \xrightarrow{\Delta G_1} *OH \xrightarrow{\Delta G_2} *O \xrightarrow{\Delta G_3} *OOH \xrightarrow{\Delta G_4} O_2$; see Section S5† for further details.[13,15,26,27] The adsorption free energies of *O, *OH and *OOH were defined using protons, electrons and water as references, and approximated as $\Delta G_{ads} \approx \Delta E_{ads} + \Delta ZPE - T\Delta S$. ΔE_{ads} is the DFT-calculated binding energy, ΔZPE is the zero-point energy change calculated with DFT using the harmonic oscillator approximation, and $T\Delta S$ are entropy corrections for H_2 and H_2O. Water–adsorbate interactions were incorporated in the form of ad hoc corrections;[28] see further details and specific values in Section S5.† The computational hydrogen electrode[29] was used to evaluate the energetics of protons and electrons. The OER overpotential is given as $\eta_{OER} = \max(\Delta G_1, \Delta G_2, \Delta G_3, \Delta G_4)/e^- - U^0$, with $U^0 = 1.23$ V *vs.* RHE.[13,15] The electrochemical step symmetry index (ESSI) is defined as $\mathrm{ESSI} = \sum_{i=1}^{n}(\Delta G_i^+)/e^- - U^0/n$. ΔG_i^+ are the free energies of the electrochemical steps larger than 1.23 eV.[30–32] The ideal catalyst has $n = 4$, $\Delta G_i^+ = 1.23$ eV, and $\eta_{OER} = \mathrm{ESSI} = 0$. Real catalysts typically have $1 \leq n \leq 3$ and highly active OER electrocatalysts are statistically inclined to display $n = 3$.[32] See further details in Section S5.†

Results and discussion

R_2NiRuO_6 oxides were synthesized by the citrate method and subsequent treatments at high temperature in air, following our previous work.[33] The structure of the R_2NiRuO_6 (R^{3+} = Pr^{3+}, Nd^{3+}, Tb^{3+}, Dy^{3+}, Y^{3+}, Ho^{3+} and Er^{3+}) double perovskites is determined by X-ray powder diffraction, as shown in Fig. 1.

To characterize the structure of the oxides in detail, Rietveld refinements of the crystal structures were performed. The oxides are in the monoclinic $P2_1/n$ space group, with long-range ordering of Ni^{2+} and Ru^{4+} at the octahedral B positions of the perovskites. Table S1† shows the unit-cell parameters and volumes obtained for each compound. The unit-cell volumes increase as the ionic radius of the rare earth increases in a pseudo-eightfold coordination environment, in the order Er^{3+} < $Y^{3+} \leq Ho^{3+} < Dy^{3+} < Tb^{3+} < Nd^{3+} < Pr^{3+}$.[34]

The OER activity of R_2NiRuO_6 is evaluated in O_2-saturated 0.1 M $HClO_4$ at 1600 rpm using a rotating disk electrode (RDE) with a geometric area of 0.196 cm^2 by recording cyclic voltammograms (CV) between 1.1 and 1.7 V *vs.* RHE at 10 mV s^{-1}. Fig. S2† shows the initial activity of the catalysts and the evolution of their activities with cycling. The currents are *iR*-corrected using the high-frequency resistance obtained from EIS (see Fig. S3†). Unlike most Ru-based perovskites, which become rapidly deactivated after a few OER cycles, the activity of R_2NiRuO_6 increases during the first cycles. In fact, the best activity is achieved after *ca.* 30 OER cycles, where the activity stabilizes (see Fig. 2a). This trend has previously been observed in certain Ru mixed oxides and has been ascribed to Ru enrichment of the surface during the first cycles (see below).[12,13] Therefore, after 30 cycles we determined the potential to reach a current density of j = 10 mA cm$_{geom}^{-2}$, which is a widely accepted figure of merit for the activity of OER catalysts.[19] The perovskite exhibiting the highest activity is Dy_2NiRuO_6, reaching a potential of 1.507 V @ 10 mA cm$_{geom}^{-2}$. The second-best catalyst is the Y-containing perovskite with *ca.* 1.6 V @ 10 mA cm$_{geom}^{-2}$. Table S2† displays the potentials needed to achieve 10 mA cm$_{geom}^{-2}$ for the studied catalysts and various state-of-the-art Ru mixed oxides, including perovskites, pyrochlores and Ru oxides. Dy_2NiRuO_6 displays a low potential, similar to that of the best reported catalysts,[15,16,35–38] which are mainly based on doped simple oxides and perovskites. We note, however, that the stability of perovskites is usually rather low in acids and visibly improved in this study.[15,16]

Fig. 2b depicts the Tafel plots for each catalyst as calculated from the 30th voltammogram. Dy_2NiRuO_6 has a slope of only 58 mV dec^{-1}, while the rest of the catalysts show slopes higher than 128 mV dec^{-1}, and Nd and Pr catalysts exhibit slopes over 200 mV dec^{-1}. These results indicate that the nature of the rare earth affects not just the activity of the perovskites, but also the OER mechanism.

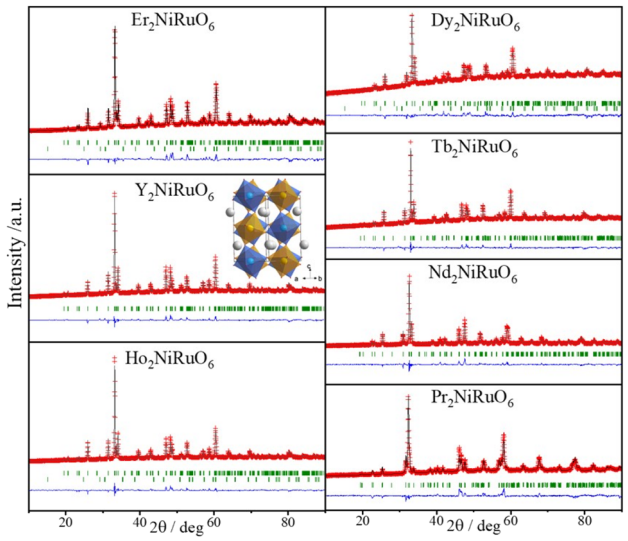

Fig. 1 Rietveld refinement of the crystal structure of R_2NiRuO_6 (R = Pr–Er) mixed oxides from XRD patterns (see Fig. S1†). The red crosses are the experimental data, the black line is for the calculated data, the blue line is the difference between experimental and calculated data and the green lines are the Bragg reflections. Er, Ho and Dy compounds show a small impurity (*ca.* 3.7%) of a second phase of $R_2Ru_2O_7$ pyrochlore (second line of Bragg reflections). The reliability factors are $R_{wp} = 7.04$ and $\chi^2 = 10.9$ for Er; $R_{wp} = 5.54$ and $\chi^2 = 9.49$ for Y; $R_{wp} = 5.93$ and $\chi^2 = 8.98$ for Ho; $R_{wp} = 3.14$ and $\chi^2 = 1.66$ for Dy; $R_{wp} = 3.82$ and $\chi^2 = 3.32$ for Tb; $R_{wp} = 6.56$ and $\chi^2 = 3.73$ for Nd; and $R_{wp} = 7.57$ and $\chi^2 = 4.77$ for Pr.

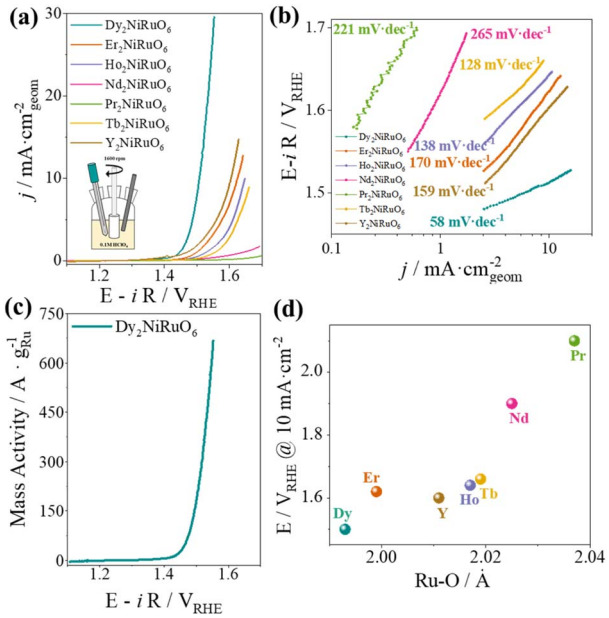

Fig. 2 (a) Polarization curves of R_2NiRuO_6 after 30 OER cycles. (b) Tafel plots of R_2NiRuO_6 after 30 OER cycles. (c) Ru mass-specific activity of Dy_2NiRuO_6. (d) Evolution of the potential at 10 mA cm^{-2} as a function of the Ru–O distances in R_2NiRuO_6.

As a first approximation to determine the intrinsic activities, the currents obtained are normalized by using the electrochemically active surface area (ECSA). ECSA values for all R_2NiRuO_6 samples range between 1.4 $m^2\ g^{-1}$ for Er_2NiRuO_6 and 8.8 $m^2\ g^{-1}$ for Dy_2NiRuO_6, which shows the highest ECSA value in the series (see Table S3†). The trends of ECSA-normalized activities for R_2NiRuO_6 (Fig. S6†), especially above 0.5 mA cm_{ECSA}^{-2}, are identical to the trend of the geometric normalized current densities (j mA cm_{geom}^{-2}). This indicates that Dy_2NiRuO_6 is indeed the most active material in the series. Fig. 2c shows the Ru mass-normalized activity of Dy_2NiRuO_6, reaching 660 A g_{Ru}^{-1} at 1.55 V. This mass activity is similar to the one reported for Y_2MnRuO_7, and greater than that of $Y_2Ru_2O_7$ (300 A g_{Ru}^{-1} at 1.55 V).[12,13]

To understand why the Dy-containing perovskite is the most active one of the series and rationalize the catalytic activity trends as a function of the rare earth (R), we correlated different crystallographic parameters with the catalytic activities. Fig. 2d shows the evolution of the potential at 10 mA cm_{geom}^{-2} as a function of the average Ru–O distances in R_2NiRuO_6 (data extracted from neutron diffraction data, ref. 33). The activity of the catalysts improves as the Ru–O distances decrease, indicating that more compact and, therefore, more hybridized Ru–O bonds are favorable for the OER. Ru–O distances are directly linked to the oxidation state of Ru through Brown's bond-valence theory, such that catalysts with shorter Ru–O bonds present higher Ru oxidation states, which tends to be beneficial for the OER.[39] In the case of Dy_2NiRuO_6, the calculated valence is +3.91.[33] In previous studies, similarly short Ru–O bonds (all around 1.98–1.99 Å) were observed in highly active OER catalysts such as $CaCu_3Ru_4O_{12}$ (ref. 35) and 3C–$SrRuO_3$.[40] Our research not only illustrates how shorter Ru–O distances lead to increased OER activity but also reveals a consistent correlation between the Ru–O bond distance and OER activity across an entire family of compounds.

The durability of the catalysts and the stability of the perovskite structure during the OER are important for the design of advanced OER catalysts in acidic electrolyte. In fact, most state-of-the-art materials, and in particular those based on Ru, are insufficiently stable during the OER in acids.[14,41] Fig. 3a shows 1000 consecutive OER cycles for Dy_2NiRuO_6 measured at 10 mV s^{-1} between 1.1 and 1.7 V *vs.* RHE. In the first OER cycle the catalyst reaches approximately 17 mA cm^{-2} at 1.55 V, increasing to almost 30 mA cm^{-2} after 100 cycles and maintaining this activity for approximately 300 cycles. To put this value into context, we remark that the durability found in Ru perovskites until this day is significantly lower, usually being active for less than 100 cycles at lower potentials (*ca.* 1.5 V *vs.* RHE), with the exception of $CaCu_3Ru_4O_{12}$, which is stable at least for 24 h at 10 mA cm^{-2},[15,35] as shown in Table S2.† We performed a chronoamperometry test of Dy_2NiRuO_6 at the potential where j ~10 mA cm^{-2}, which is *ca.* 1.55 V (Fig. S7†). After 5 h the activity decays by *ca.* 25%. However, we cannot ascribe this activity loss only to the deactivation of the catalyst. The profuse formation of bubbles leads to the physical detachment of the catalyst from the electrode. This feature is, at least in part, also responsible for the observed activity loss.

We evaluated the durability of the other members of the series by performing OER cycling. Fig. S2† shows the activity after 1, 10, 20, 30 and 100 OER cycles of R_2NiRuO_6. Fig. 3b shows the percentage of OER activity gained or lost, measured as the shift in current density at the same potential between the first and 30th OER cycles. Dy_2NiRuO_6 is the most durable catalyst with an increment in activity not only during the first 30

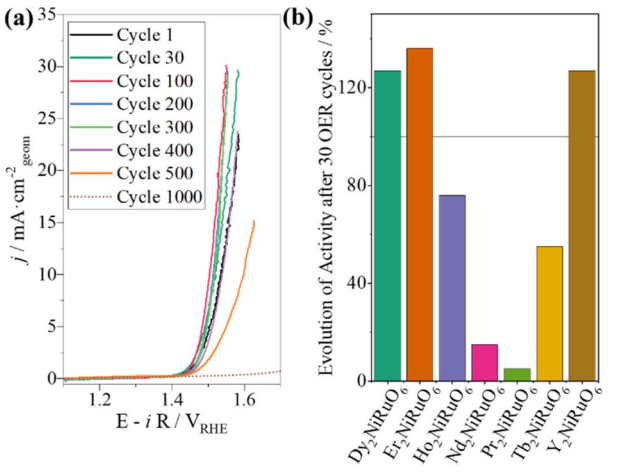

Fig. 3 (a) 1000 OER cycles measured at 10 mV s^{-1} between 1.1 and 1.7 V for Dy_2NiRuO_6. (b) Evolution of the OER activity measured as the shift in current density at the same potential (1.7 V not *i*R corrected) from the first cycle to the 30th one, measured at 10 mV s^{-1} between 1.1 and 1.7 V *vs.* RHE. For Pr_2NiRuO_6 the second cycle was used instead of the first one for the calculation, due to the large decrease in activity on the Pr sample after the first cycle, suggesting that the initial activity is mainly related to corrosion.

cycles but up to the first 100 cycles, followed by Y_2NiRuO_6, which is active for 500 cycles. The other members of the series, with R = Er, Ho, Tb, Nd and Pr, tend to be unstable. For instance, Ho_2NiRuO_6 and Tb_2NiRuO_6 lose 26 and 46% of their activity after 30 cycles, respectively, and completely lose their activities after 100 cycles. These results indicate that the crystallographic parameters influencing the catalytic activity also affect the durability/stability. For instance, the evolution of the durability with Ru–O bond distances is similar to the trend with the activity, indicating that shorter Ru–O bonds are also beneficial for the durability. Again, shorter bond distances translate into a slightly higher Ru oxidation state. Interestingly, it has previously been reported that higher Ru oxidation states are beneficial for the durability of Ru perovskites.[15,16]

Once we ascertained that Dy_2NiRuO_6 is the most active and durable catalyst in the series, we studied its structural changes during the OER. First, we studied the evolution of the surface area of Dy_2NiRuO_6 with increasing number of OER cycles. For this measurement we used the surface area values as determined from EIS; see the ESI.† As shown in Fig. S5,† the surface area decreases from approximately 17 to 13 $m^2\ g^{-1}$ during the first 100–150 cycles, and this value is maintained during the following cycles, indicating that the surface is already reconstructed after 150 cycles. Additionally, if the EIS measurements are performed at a potential at which the OER occurs, information on the kinetics of the reaction can be obtained from the charge transfer resistance (R_{ct}).[42] As expected from the enhancement of the activity in the first cycles, R_{ct} decreases as the activity increases during the first cycles (Fig. S3†).

We also considered the morphological, compositional and structural variations in Dy_2NiRuO_6 during the OER. The cycled samples are referred to as *N*-Dy_2NiRuO_6, where *N* is the number of cycles. First, the evolution of the crystal structure of Dy_2NiRuO_6 was investigated by means of XRD. Fig. 4a shows the XRD patterns of Dy_2NiRuO_6, 100-Dy_2NiRuO_6, 500-Dy_2NiRuO_6, 700-Dy_2NiRuO_6 and 1000-Dy_2NiRuO_6. The perovskite structure is maintained over the 1000 OER cycles, without the formation of secondary crystalline phases but with a larger amorphous component when the cycles increase (especially observed for 1000-Dy_2NiRuO_6).

Representative TEM images for the initial-Dy_2NiRuO_6 are shown in Fig. 4b and S8.† As observed, initial-Dy_2NiRuO_6 has a mean particle size of 177(6) nm. The atomic composition obtained by EDX is $Dy_{1.8(2)}Ni_{1.1(1)}Ru_{1.1(1)}O_x$, which is close to the nominal stoichiometric value. Besides, a few particles without nickel, ascribed to the presence of $Dy_2Ru_2O_7$ pyrochlore, can be observed. This phase is also detected by the XRD refinement as a minor impurity (close to 4 % wt). Fig. 4b also shows representative TEM images of 100-Dy_2NiRuO_6 and 1000-Dy_2NiRuO_6. In 100-Dy_2NiRuO_6 the particles remain stable and the size and morphology are similar to those of initial-Dy_2NiRuO_6.

Nevertheless, a careful inspection of the TEM images of 100-Dy_2NiRuO_6 reveals the presence of a few small particles, probably indicative of an incipient degradation process. As shown in Fig. S9,† a number of small spherical particles in the periphery of well-defined larger particles can be observed. The presence of these small particles becomes more evident in 1000-Dy_2NiRuO_6,

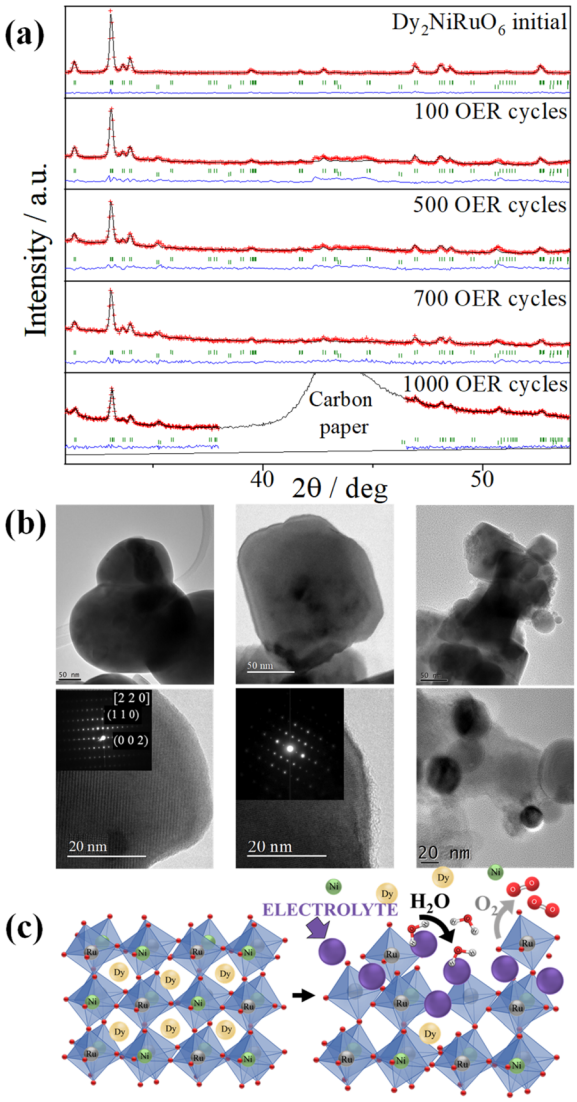

Fig. 4 (a) XRD data and Rietveld refinement of the crystal structure of Dy_2NiRuO_6 upon cycling. The broad peak between *ca.* 40 and 47° in the diffractogram of the sample after 1000 cycles is due to carbon. Reliability factors: $R_{wp} = 3.14$ and $\chi^2 = 1.66$ for the initial catalyst; $R_{wp} = 5.27$ and $\chi^2 = 5.12$ for the catalyst after 100 cycles; $R_{wp} = 4.01$ and $\chi^2 = 2.56$ for the catalyst after 500 cycles; $R_{wp} = 3.01$ and $\chi^2 = 3.92$ for the catalyst after 700 cycles; and $R_{wp} = 2.00$ and $\chi^2 = 2.47$ for the catalyst after 1000 cycles. (b) Upper panel: TEM images. Lower panel: HRTEM, ED and TEM images. Left: initial-Dy_2NiRuO_6. Middle: 100-Dy_2NiRuO_6. Right: 1000-Dy_2NiRuO_6. (c) Schematics of the processes occurring on the catalyst surface during the OER.

where the larger particles also become more irregular, with less smooth and rougher borders (Fig. 4b, right middle panel).

Fig. 4b (lower panel) shows representative HRTEM images and electron diffraction patterns (ED, inset) for the fresh and used catalyst. Initial-Dy_2NiRuO_6 is a crystalline material with diffraction spots ascribed to the (110) and (002) planes of the perovskite structure (inset of the left lower panel). In 100-Dy_2NiRuO_6, the crystallographic structure within the particles remains crystalline with well-defined diffraction spots corresponding to the initial perovskites (inset of the middle lower

panel). However, the 100-Dy_2NiRuO_6 surface is slightly rougher than that in Dy_2NiRuO_6, indicating a higher level of disorder of the atoms located at the periphery of the particles. In 1000-Dy_2NiRuO_6, it is not possible to detect crystallographic planes in the larger particles, indicating that the catalyst loses its crystallinity as a result of its severe degradation. However, by means of XRD it is still possible to detect perovskite reflections merged with a large amorphous component.

EDX analyses were performed to determine the composition of the cycled catalyst. In 100-Dy_2NiRuO_6, the atomic values are 50.7% for Dy, 26.6% for Ni, and 22.7% for Ru (similar to those of the initial catalyst, see above). Two types of particles are observed in 1000-Dy_2NiRuO_6: (i) large particles, corresponding to the original perovskite, with a composition of 51.9% for Dy, 7.1% for Ni, and 41.1% for Ru, indicating that most of the Ni is lost in such particles; (ii) small particles, which are only composed of Ni, probably as Ni–O, Ni–OH and/or Ni–OOH particles. These particles are formed as a result of the dissolution and redeposition of Ni during the OER.

The surface composition of initial-Dy_2NiRuO_6, and the environment and oxidation states of Dy, Ru and Ni cations were studied by XPS. The Ru_{3d} + C_{1s} core-level regions of the XPS spectrum are shown in Fig. 5a. The strong peak at 284.6 eV is ascribed to C 1s. In addition, a minor contribution of C–O and C═O species results in a broad peak at *ca.* 289 eV. The presence of Ru is deduced from the Ru $3d_{5/2}$ peak at *ca.* 281.9 eV (green peak in Fig. 5a). This binding energy (BE) is usually ascribed to oxidized Ru species, typically Ru^{4+}, in good agreement with the expected oxidation state of Ru cations in Dy_2NiRuO_6. The XPS spectrum of 100-Dy_2NiRuO_6 is shown in Fig. 5b. A single Ru species with the Ru $3d_{5/2}$ peak at *ca.* 281.9 eV is observed, suggesting that the catalyst remains stable during cycling, in agreement with our TEM and XRD analyses. Conversely, the spectra of 500-Dy_2NiRuO_6 and 1000-Dy_2NiRuO_6 display two Ru species, with Ru $3d_{5/2}$ peaks at *ca.* 281.6 and 282.7 eV. The first peak characterizes the original Ru^{4+} species, whereas the latter peak at 282.7 eV is usually ascribed in the literature to Ru^{3+} species.[43] In view of these assignments, and taking into account the environment in which the OER cycles are recorded, we assign the Ru peaks observed in the spectra of 500-Dy_2NiRuO_6 and 1000-Dy_2NiRuO_6 to Ru^{3+} species, probably Ru hydroxides.

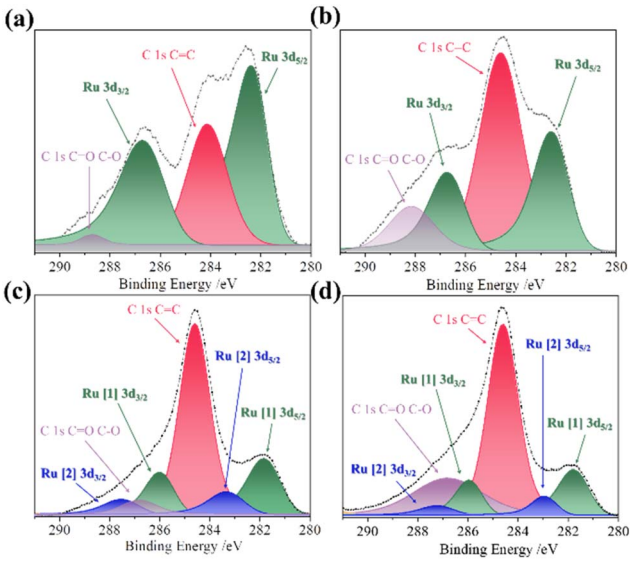

Fig. 5 XPS of the Ru 3d + C 1s core-level region of (a) initial-Dy_2NiRuO_6, (b) 100-Dy_2NiRuO_6, (c) 500-Dy_2NiRuO_6 and (d) 1000-Dy_2NiRuO_6.

XPS also shows that the relative surface concentration of Ru varies during the OER, as shown in Table S4.† First of all, a clear dissolution of Dy occurs from the beginning of the reaction but becomes more evident after 500 cycles. The atomic surface ratio for Ru/Ni evolves more slowly, as it increases from 1.9 in Dy_2NiRuO_6 to 4.1 in 100-Dy_2NiRuO_6, and remains roughly constant in 500-Dy_2NiRuO_6, with an atomic Ru/Ni ratio of 4.3. This ratio decreases with further cycling to a value of 2.3 in 1000-Dy_2NiRuO_6. This trend suggests that the increment of the initial activity is related mainly to the dissolution of Dy cations, together with a slight enrichment of Ru at the surface, which is still rich in both Ru and Ni during the OER. Surface reconstruction occurs in numerous OER catalysts in view of the harsh reaction conditions. In fact, Ru enrichment has been previously reported in acids for Ru-based catalysts such as pyrochlores.[13,44] After 1000 cycles measured at 10 mV s^{-1} the perovskite phase loses its crystallinity and most Ni atoms are gone, segregated into small Ni-based particles, which evinces the catalyst degradation.

To supplement our experimental findings, we carried out a computational analysis of the OER performance of the most active double perovskite in this study, namely Dy_2NiRuO_6, and compared it to that of other state-of-the-art Ru and Ir perovskites. Fig. 6 shows the trends in OER overpotential (η_{OER}) as a function of the free energy difference of the key intermediates *O and *OH. We observe in Fig. 6 that the contribution of Ni sites to the overall OER activity is likely small, as they lie on the weak-binding side of the plot, far from the apex. Conversely, Ru sites are initially rather active and display a compromise between the energies of the two likely potential-limiting steps. In addition, their activity increases slightly upon Dy dissolution. In fact, the predicted activity in Fig. 6 of Ru sites upon Dy dissolution matches the experimental one, which was added to the plot following the semiempirical method by Jaramillo and coworkers.[15,26] Previous statistical analysis showed that the most likely potential-limiting steps of the OER can either be the second or third electrochemical steps, namely, *OH dehydrogenation for weak-binding sites, or *OOH formation for strong-binding sites[45] (eqn S2 and S3 in the ESI†). As shown in Table S5,† Ni sites are limited by *OH dehydrogenation, while Ru sites with less Ni or no Ni around are limited by *OOH formation. Besides, Ru sites with a stoichiometric proportion of Ni : Ru are close to the top of the volcano and, hence, can be limited by either step.

However, the OER activity decreases when the content of Ni is progressively lost at the surface ("less Ni" and "no Ni" data in Fig. 6). This means that, although Ru sites are the actual active sites and Ni sites are not active, which is expected since Ni is only active for the OER in alkaline media,[46,47] their proximity to Ru sites is key to the OER activity. Interestingly, Fig. 6 shows

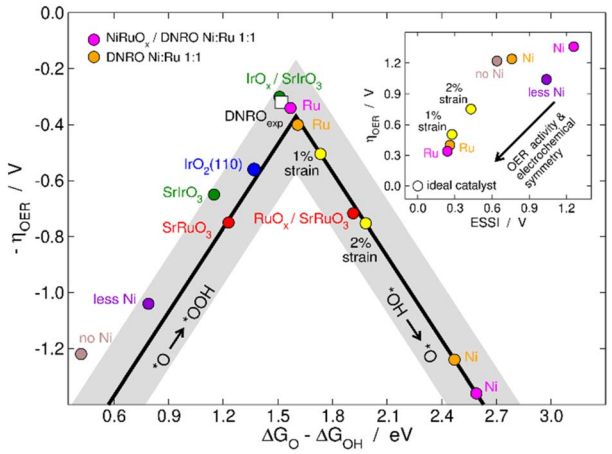

Fig. 6 Sabatier-type activity plot for the OER on various perovskites. Ni and Ru sites on pristine Dy_2NiRuO_6 (referred to as DNRO) are shown in orange. Ni and Ru sites on a $NiRuO_x$ overlayer formed upon Dy^{3+} dissolution (referred to as $NiRuO_x$/DNRO) are shown in fuchsia. Data for $NiRuO_x$/DNRO with 1 and 2% stretching strain are shown in yellow. Experimental data ($DNRO_{exp}$, white square) were added through a method described elsewhere.[15,26] "Less Ni" is $NiRuO_x$/DNRO with a local surface content of Ni that is three times lower than that of Ru. "No Ni" is RuO_x/DNRO, which has no nickel at the surface, see Section S2.† Literature data are also provided for $SrRuO_3$ and $RuO_x/SrRuO_3$,[15] $SrIrO_3$ and $IrO_x/SrIrO_3$,[27] and IrO_2(110).[48] Inset: OER overpotential as a function of the electrochemical-step symmetry index (ESSI) of the active sites. As the active sites become more symmetric (low values of ESSI), the OER overpotential decreases. The ideal catalyst (ESSI = η_{OER} = 0) is shown for comparison.

that when Ni is lost, Ru sites bind the OER intermediates too strongly. This is in line with the facts that RuO_x overlayers on $SrRuO_3$ have low OER activity[15] and that Mn was also recently found to enhance the activity of RuO_x overlayers on Y_2MnRuO_7.[13] Conversely, IrO_x overlayers on $SrIrO_3$ display salient OER activity without any other element in the structure.[27]

Overall, it seems that Ni induces an electronic effect that progressively weakens the adsorption energies of *O, *OH, and *OOH on Ru sites. To rationalize this activity trend, we resorted to a descriptor called the electrochemical-step symmetry index (ESSI),[30–32] the values of which indicate how energetically symmetric an electrocatalyst is, as shown in the Computational modelling section and Section S5.† As the ESSI tends to zero, the OER overpotential should also tend to zero. This is illustrated in the inset of Fig. 6, where Ni sites are rather asymmetric and so are Ru sites with little or no Ni content in the vicinities. In contrast, Ru sites located at catalyst regions in which the Ni : Ru ratio is 1 : 1 are highly symmetric and, hence, display low OER overpotentials.

We also investigated the effect of Ru–O distances on the OER. In line with the experimental results in Fig. 2d, as the equilibrium Ru–O distances are stretched by 1 and 2%, η_{OER} increases from 0.34 to 0.50 and 0.75 V, as shown in Fig. 6. The overpotential increases because stretching the Ru–O distances progressively weakens the adsorption energies of *O, *OH, and *OOH, as shown in Table S5.† In addition, the inset of Fig. 6 shows that strain in this case decreases the electrochemical symmetry of the active sites.

In sum, our DFT-based modelling suggests that to reach a high initial OER activity of Dy_2NiRuO_6 one should guarantee that the local ratio of Ni : Ru is 1 : 1. Besides, to maintain the activity as high as possible upon cycling it is instrumental to avoid the loss of Ni.

Conclusions

We showed a significant enhancement of the durability of Ru perovskites for the OER in acid media for R_2NiRuO_6. The use of rare earths, instead of alkali and alkaline earth metals in perovskite oxides is a suitable way to increase the stability and durability of the catalysts.

Among the studied perovskites, Dy_2NiRuO_6 exhibits the greatest activity and durability, needing only 1.507 V to achieve 10 mA cm^{-2} and being active for approximately 500 cycles measured at 10 mV s^{-1} and up to 1.7 V. The reason for the higher performance of Dy_2NiRuO_6 compared to the rest of the series is presumably related to shorter Ru–O bonds in the crystal structure, which suggests more hybridization, a higher Ru oxidation state and suitable adsorption energies of the OER intermediates. Furthermore, computational modelling showed that the high OER activity of Dy_2NiRuO_6 is related to the presence of Ru active sites, but also that a local ratio of Ni : Ru close to 1 : 1 is beneficial for the OER, while the experimentally observed catalyst deactivation is likely linked to Ni surface segregation, dissolution and redeposition to form Ni particles. Hence, future studies could focus on preventing Ni losses upon OER cycling. All in all, this work opens a route to search for more durable perovskites with low Ru content for the OER in acidic media for PEM electrolyzers.

Conflicts of interest

There are no conflicts to declare.

Acknowledgements

This work was funded by the PROMET-H2 project from the European Union Horizon 2020 research and innovation programme under grant agreement No. 862253; also, by the Deputyship for Research & Innovation, Ministry of Education of Saudi Arabia for the project number 341; and by the Spanish grants TED2021-131033B-I00, TED2021-132550B-C21, PID2020-116712RB-C21, PID2021-122477OB-I00 and PID2021-127957NB-I00 from MCIN/AEI/10.13039/501100011033. A. T.-M. thanks the Consejería de Educación, Juventud y Deporte of the Comunidad de Madrid for the Ayuda Destinada a la Atracción de Talento Investigador (2020-T2/AMB-19927). I. R.-G. thanks the PhD Program in Electroquímica, Ciencia y Tecnología of Escuela de doctorado of Universidad Autónoma de Madrid. FCV also acknowledges financial support through grant IT1453-22 "Grupos Consolidados UPV/EHU del Gobierno Vasco" and thanks the Red Española de Supercomputación for computational resources (grant QHS-2023-3-0019). The use of

supercomputing facilities at SURFsara was sponsored by NWO Physical Sciences, with financial support by NWO.

Notes and references

1 IRENA, *Green Hydrogen Cost Reduction. Scaling up Electrolysers to Meet the 1.5°C Climate Goal*, 2020.
2 T. Reier, M. Oezaslan and P. Strasser, *ACS Catal.*, 2012, **2**, 1765–1772.
3 I. Katsounaros, S. Cherevko, A. R. Zeradjanin and K. J. J. J. Mayrhofer, *Angew. Chem., Int. Ed.*, 2014, **53**, 102–121.
4 S. Shiva Kumar and V. Himabindu, *Mater. Sci. Energy Technol.*, 2019, **2**, 442–454.
5 G. S. Ogumerem and E. N. Pistikopoulos, *J. Process Control*, 2020, **91**, 37–49.
6 M. Retuerto, L. Pascual, J. Torrero, M. A. Salam, Á. Tolosana-Moranchel, D. Gianolio, P. Ferrer, P. Kayser, V. Wilke, S. Stiber, V. Celorrio, M. Mokthar, D. G. Sanchez, A. S. Gago, K. A. Friedrich, M. A. Peña, J. A. Alonso and S. Rojas, *Nat. Commun.*, 2022, **13**, 7935.
7 J. Torrero, T. Morawietz, D. García Sanchez, D. Galyamin, M. Retuerto, V. Martin-Diaconescu, S. Rojas, J. A. Alonso, A. S. Gago and K. A. Friedrich, *Adv. Energy Mater.*, 2023, **13**, 1–13.
8 N. Hodnik, P. Jovanovič, A. Pavlišič, B. Jozinović, M. Zorko, M. Bele, V. S. Šelih, M. Šala, S. Hočevar and M. Gaberščček, *J. Phys. Chem. C*, 2015, **119**, 10140–10147.
9 Q. Feng, Q. Wang, Z. Zhang, Y. Xiong, H. Li, Y. Yao, X. Z. Yuan, M. C. Williams, M. Gu, H. Chen, H. Li and H. Wang, *Appl. Catal., B*, 2019, **244**, 494–501.
10 J. Kim, P. C. Shih, K. C. Tsao, Y. T. Pan, X. Yin, C. J. Sun and H. Yang, *J. Am. Chem. Soc.*, 2017, **139**, 12076–12083.
11 J. Kim, P. Shih, Y. Qin, Z. Al-Bardan, C. Sun and H. Yang, *Angew. Chem., Int. Ed.*, 2018, **57**, 13877–13881.
12 M. A. Hubert, A. M. Patel, A. Gallo, Y. Liu, E. Valle, M. Ben-Naim, J. Sanchez, D. Sokaras, R. Sinclair, J. K. Nørskov, L. A. King, M. Bajdich and T. F. Jaramillo, *ACS Catal.*, 2020, 12182–12196.
13 D. Galyamin, J. Torrero, I. Rodríguez, M. J. Kolb, P. Ferrer, L. Pascual, M. A. Salam, D. Gianolio, V. Celorrio, M. Mokhtar, D. Garcia Sanchez, A. S. Gago, K. A. Friedrich, M. A. Peña, J. A. Alonso, F. Calle-Vallejo, M. Retuerto and S. Rojas, *Nat. Commun.*, 2023, **14**, 2010.
14 B.-J. Kim, D. F. Abbott, X. Cheng, E. Fabbri, M. Nachtegaal, F. Bozza, I. E. Castelli, D. Lebedev, R. Schäublin, C. Copéret, T. Graule, N. Marzari and T. J. Schmidt, *ACS Catal.*, 2017, **7**, 3245–3256.
15 M. Retuerto, L. Pascual, F. Calle-Vallejo, P. Ferrer, D. Gianolio, A. G. Pereira, Á. García, J. Torrero, M. T. Fernández-Díaz, P. Bencok, M. A. Peña, J. L. G. Fierro and S. Rojas, *Nat. Commun.*, 2019, **10**, 2041.
16 I. Rodríguez-García, D. Galyamin, L. Pascual, P. Ferrer, M. A. Peña, D. Grinter, G. Held, M. Abdel Salam, M. Mokhtar, K. Narasimharao, M. Retuerto and S. Rojas, *J. Power Sources*, 2022, **521**, 230950.
17 H. M. Rietveld, *J. Appl. Crystallogr.*, 1969, **2**, 65–71.
18 R. Dinnebier and J. Rodríguez-carvajal, *Commission on Powder Diffraction. Rietveld Refinement from Powder Diffraction Data CPD Chairman's Message 26 CPD Projects from the Editor of Newsletter*, vol. 26, 2001.
19 C. C. L. L. McCrory, S. Jung, J. C. Peters and T. F. Jaramillo, *J. Am. Chem. Soc.*, 2013, **135**, 16977–16987.
20 G. Kresse and J. Furthmüller, *Phys. Rev. B: Condens. Matter Mater. Phys.*, 1996, **54**, 11169–11186.
21 J. P. Perdew, K. Burke and M. Ernzerhof, *Phys. Rev. Lett.*, 1996, **77**, 3865.
22 G. Kresse and D. Joubert, *Phys. Rev. B*, 1999, **59**, 1758–1775.
23 S. L. Dudarev, G. A. Botton, S. Y. Savrasov, C. J. Humphreys and A. P. Sutton, *Phys. Rev. B*, 1998, **57**, 1505–1509.
24 Z. Xu, J. Rossmeisl and J. R. Kitchin, *J. Phys. Chem. C*, 2015, **119**, 4827–4833.
25 F. Zhou, M. Cococcioni, C. A. Marianetti, D. Morgan and G. Ceder, *Phys. Rev. B*, 2004, **70**, 235121.
26 Z. W. Seh, J. Kibsgaard, C. F. Dickens, I. Chorkendorff, J. K. Nørskov and T. F. Jaramillo, *Science*, 2017, **355**, eaad4998.
27 L. C. Seitz, C. F. Dickens, K. Nishio, Y. Hikita, J. Montoya, A. Doyle, C. Kirk, A. Vojvodic, H. Y. Hwang, J. K. Norskov and T. F. Jaramillo, *Science*, 2016, **353**, 1011–1014.
28 F. Calle-Vallejo, A. Krabbe and J. M. García-Lastra, *Chem. Sci.*, 2016, **8**, 124–130.
29 J. K. Nørskov, J. Rossmeisl, A. Logadottir, L. Lindqvist, J. R. Kitchin, T. Bligaard and H. Jónsson, *J. Phys. Chem. B*, 2004, **108**, 17886–17892.
30 N. Govindarajan, J. M. García-Lastra, E. J. Meijer and F. Calle-Vallejo, *Curr. Opin. Electrochem.*, 2018, **8**, 110–117.
31 O. Piqué, F. Illas and F. Calle-Vallejo, *Phys. Chem. Chem. Phys.*, 2020, **22**, 6797–6803.
32 E. Romeo, F. Illas and F. Calle-Vallejo, *Chem. Sci.*, 2023, **14**, 3622–3629.
33 P. Kayser, J. A. Alonso, A. Muñoz and M. T. Fernández-Díaz, *Acta Mater.*, 2017, **126**, 114–123.
34 R. D. Shannon, *Acta Crystallogr., Sect. A: Cryst. Phys., Diffr., Theor. Gen. Crystallogr.*, 1976, **32**, 751–767.
35 X. Miao, L. Zhang, L. Wu, Z. Hu, L. Shi and S. Zhou, *Nat. Commun.*, 2019, **10**, 1–7.
36 Y. Lin, Z. Tian, L. Zhang, J. Ma, Z. Jiang, B. J. Deibert, R. Ge and L. Chen, *Nat. Commun.*, 2019, **10**(1), 162.
37 S. Hao, M. Liu, J. Pan, X. Liu, X. Tan, N. Xu, Y. He, L. Lei and X. Zhang, *Nat. Commun.*, 2020, **11**, 5368.
38 C. Lin, J.-L. Li, X. Li, S. Yang, W. Luo, Y. Zhang, S.-H. Kim, D.-H. Kim, S. S. Shinde, Y.-F. Li, Z.-P. Liu, Z. Jiang and J.-H. Lee, *Nat. Catal.*, 2021, **4**, 1012–1023.
39 I. D. Brown and R. D. Shannon, *Acta Crystallogr.*, 1973, **29**, 266.
40 S. H. Chang, J. G. Connell, N. Danilovic, R. Subbaraman, K. C. Chang, V. R. Stamenkovic and N. M. Markovic, *Faraday Discuss.*, 2014, **176**, 125–133.
41 N. Danilovic, R. Subbaraman, K. C. Chang, S. H. Chang, Y. J. Kang, J. Snyder, A. P. Paulikas, D. Strmcnik, Y. T. Kim, D. Myers, V. R. Stamenkovic and N. M. Markovic, *J. Phys. Chem. Lett.*, 2014, **5**, 2474–2478.
42 A. Lasia, *J. Phys. Chem. Lett.*, 2022, **13**, 580–589.

43 D. J. Morgan, *Surf. Interface Anal.*, 2015, **47**, 1072–1079.
44 M. A. Hubert, A. M. Patel, A. Gallo, Y. Liu, E. Valle, M. Ben-Naim, J. Sanchez, D. Sokaras, R. Sinclair, J. K. Nørskov, L. A. King, M. Bajdich and T. F. Jaramillo, *ACS Catal.*, 2020, **10**, 12182–12196.
45 E. Sargeant, F. Illas, P. Rodríguez and F. Calle-Vallejo, *J. Electroanal. Chem.*, 2021, **896**, 115178.
46 X. Hou, T. Jiang, X. Xu, X. Wang, J. Zhou, H. Xie, Z. Liu, L. Chu and M. Huang, *Chin. J. Struct. Chem.*, 2022, **41**, 2207074–2207080.
47 J. Mohammed-Ibrahim, *J. Power Sources*, 2020, **448**, 227375.
48 I. C. Man, H. Y. Su, F. Calle-Vallejo, H. A. Hansen, J. I. Martínez, N. G. Inoglu, J. Kitchin, T. F. Jaramillo, J. K. Nørskov, J. Rossmeisl, F. Calle-Vallejo, H. A. Hansen, J. I. Martínez, N. G. Inoglu, J. Kitchin, T. F. Jaramillo, J. K. Nørskov and J. Rossmeisl, *ChemCatChem*, 2011, **3**, 1159–1165.